VALIDATION OF LOW PRESSURE TURBINE CASCADE

Arzu İsmi*, Batuhan Şahin, Oğuzhan Çamlıca, Berati M. Kılıç

Ankara Yıldırım Beyazıt University, Ankara, Türkiye

ABSTRACT

This study investigates the aerodynamic performance of a linear cascade of a low-pressure turbine (LPT) blade, specifically the T106A cascade, through steady-state computational fluid dynamics (CFD) simulations. Two-dimensional (2D) and three-dimensional (3D) simulations were conducted using the Reynolds-Averaged Navier-Stokes (RANS) equations, with different turbulence model implemented in ANSYS. The simulations focused on predicting pressure coefficient distributions along the blade surface, which were subsequently validated against experimental data. We compare the pressure coefficient values obtained from 2D simulations with experimental data for three different viscosity models: k-omega, k-epsilon, and Spalart-Allmaras. For the 3D simulations, only the Spalart-Allmaras model was utilized. The comparison highlights the accuracy and limitations of the RANS approach in capturing key flow features, such as boundary layer behavior and flow separation, in LPT cascades. These findings provide insights into the applicability of the Spalart-Allmaras model for turbine blade design and performance prediction. Additionally, the study examines kinetic energy losses (KE losses) in the turbine cascade, categorizing them into major losses, such as flow separation and wake mixing, and minor losses, including secondary flows and endwall effects. The impact of these losses on the overall aerodynamic efficiency of the blade cascade is discussed in the context of the simulation results.

Keywords: Low pressure turbine, CFD, Turbulence models, Turbine Losses

NOMENCLATURE

Roman letters

C	Chord length [mm]
C_x	Axial chord length [mm]
KE	Kinetic energy
k	Turbulent kinetic energy [m^2/s^2]
S	Mean rate-of-strain tensor [1/s]
P	Pitch [mm]
b	Span [mm]
p	Pressure [Pa]
p_t	Total pressure [Pa]

Greek letters

α_1	Inlet flow angle [degrees]
α_2	Design exit flow angle [degrees]
ρ	Density [kg/m^3]
ν	Kinematic viscosity [m^2/s]
ν_t	Turbulent eddy viscosity [m^2/s]
τ_w	Wall shear stress [Pa]
ω	Specific dissipation rate [1/s]
ϵ	Turbulence dissipation rate [m^2/s^{-3}]

Dimensionless groups

ζ	Kinetic energy loss coefficient
y^+	Dimensionless wall distance
κ	Von Kármán constant
Pr	Prandtl number
Re	Reynolds number
Sc	Schmidt number
C_p	Pressure coefficient
C_f	Skin friction coefficient

Superscripts and subscripts

∞	Free stream value
$\bar{\cdot}$	Mean value

1. INTRODUCTION

In modern gas turbines, low pressure turbines (LPT) have a critical role in the overall efficiency and weight of the engine. In LPT Deceleration designs, maintaining the precise balance between lift and loss balance is of great importance to optimize the aerodynamic performance of the turbine. However, secondary flows and boundary layer Decoupling occurring in LPT wings are among the main causes of aerodynamic losses. This situation negatively affects the energy efficiency and overall performance of the turbine.

In this context, understanding the flow structure and loss mechanisms in LPT flaps is important for developing more efficient designs. Low-resolution simulations and experimental studies conducted with the Reynolds-Averaged Navier-Stokes (RANS) approach are available in the literature. However, these studies provide limited information about the detailed physics of secondary losses and the effects of different input conditions (for example, laminar/turbulent boundary layer).

*Corresponding author: 20110111016@aybu.edu.tr
Documentation for `asmeconf.cls`: Version 1.38, December 22, 2024.

1.1 Purpose

This project aims to study the 2D and 3D flow structures in detail in order to improve the aerodynamic performance of LPT wings. In this context:

- Steady-state CFD simulations will be performed on a linear array of low-pressure turbine blades using Reynolds-Averaged Navier-Stokes (RANS) equations.

- Simulations will be carried out with different turbulence modeling strategies and the effects of these models will be analyzed.

- The results obtained will be verified by experimental data or high-resolution simulations (DNS or LES).

1.2 Low Pressure Turbine

In modern propulsion systems, the low pressure turbines are significant components, undertaking the mission in driving the rotational components, fan and compressor. Also, the low pressure turbine can be used as power output mechanism, that supplies the shaft power to drive a propeller or any kind of lift or thrust machine. In the engine, the low pressure turbine locates behind the high pressure turbine, if flow direction is accepted as reference [1]. In Figure 1, the gas turbine engine and location of components illusturated.

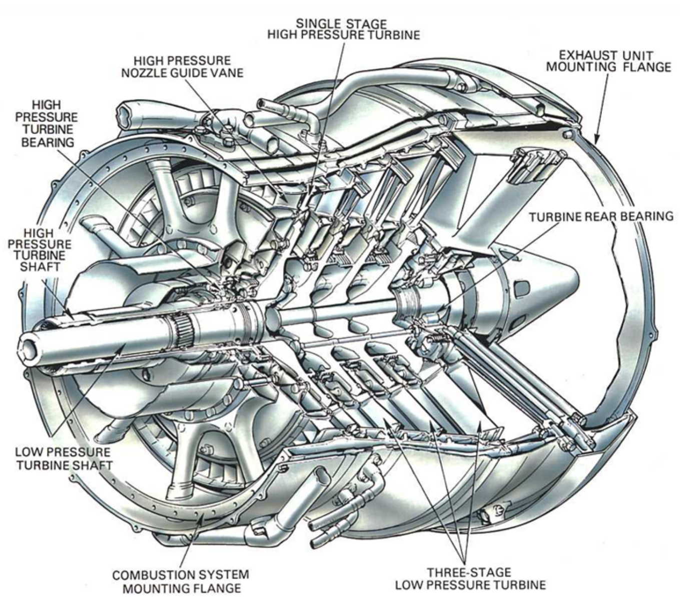

FIGURE 1: A TWIN TURBINE AND SHAFT ARRANGEMENT. [2]

The specific fuel consumption of an engine is greatly effected by the efficiency of low pressure turbine. The 1% increase of low pressure polytropic efficiency causes to 0.5-1.0% increase of specific fuel consumption. Because of that low pressure turbine been multiple stages, the weight of LPT is one third or one fifth of total weight of engine. Also, higher number of low pressure turbine stages cause to increase of manufacturing complexity[3].

1.3 Losses in Turbine Cascades

Gas turbines are high-capacity machines that play a critical role in modern energy production and industrial applications. A significant portion of the world's energy is generated through these machines. In addition to their use in energy production facilities, gas turbines are widely utilized in the aviation and maritime sectors. The high efficiency of these machines not only provides economic benefits but also enhances key performance parameters such as power capacity, range, and overall performance. Consequently, minimizing turbine losses and improving efficiency are primary objectives in the design of gas turbine stages.

Losses occurring in the turbine section of a gas turbine are among the most significant factors adversely affecting the overall performance of the machine. The flow in a turbine stage is inherently three-dimensional, viscous, turbulent, and compressible. These complex flow characteristics lead to entropy generation during operation, which directly contributes to energy losses. The primary factors causing entropy increase include viscous friction within boundary layers, instabilities arising from the mixing of high- and low-pressure fluids, the presence of shock waves, and heat transfer between the flow and surrounding components. Each of these factors contributes to an increase in losses, negatively impacting turbine performance [4].

In this context, efforts to minimize these losses are of great importance in gas turbine design. Improvements achieved by considering both fluid dynamics and thermodynamic effects significantly enhance the efficiency of gas turbines, reduce energy production costs, and contribute to meeting performance targets effectively [4].

Before CFD simulations, aerodynamics experts should work on estimating the significance of major component losses which are necessary for the one-dimensional meanline calculations. To achieve this, experimental, semi-experimental and theoretical loss correlations are used. These correlations might be established by research centers or manufacturers. This is interestingly observed, the measured efficiencies do not vary significantly for different correlations which have different concepts and philosophies [5]. As stated in Traupel's [6] book, a turbomachinery stage can achieve an efficiency of 85%, with five major loss sources, each contributing an uncertainty of ±20%. Combined, these result in a total uncertainty of ±10% for the loss coefficient. Given the normalized loss coefficient (15%), the resulting efficiency uncertainty is approximately 1.5%, which is acceptable for preliminary calculations. Thus, loss correlations are integral to the design process. The major aerodynamic losses are:

- Profile or primary loss

- Loss due to the trailing edge thickness

- Secondary flow loss

- Loss due to trailing edge mixing in cooled gas turbine blades

- Exit loss
- Minor loss

Minor losses involves disc friction and wetness losses. Wetness loss is peculiar to steam turbine design.

1.3.1 Turbine Profile Loss. "The profile losses are caused, among others, by the Reynolds- and Mach-number effects, geometry parameters, such as chord-spacing ratio c/s, maximum blade thickness-chord ratio t/c, and surface roughness"[5]. In intermediate turbine (IPT) and low pressure turbine, blade thickness is decrease from hub to tip because there is highly mechanical stress in the hub.

1.3.2 Stage Profile Losses. Stage profile loss refers to the total aerodynamic loss in a turbine stage, which is caused by various factors such as flow separation, mixing, and viscous effects. These losses are typically quantified using the entropy difference between the inlet and outlet or through the use of stage loss coefficients. The stage loss coefficient provides a practical way to assess the aerodynamic efficiency of the turbine stage by normalizing the pressure difference to reference conditions.

These losses are important in determining the row efficiency, which reflects how effectively the turbine row converts energy into useful work. Minimizing stage profile losses is critical for improving the overall performance and efficiency of the turbine. The calculation of these losses, using either entropy differences or loss coefficients, helps in identifying areas where aerodynamic improvements can be made to reduce dissipation and increase the energy conversion efficiency [5].

1.3.3 Trailing Edge Thickness Loss. The downstream of a stator or a rotor cascade, the trailing edge thickness gives rise to a reduction in exit velocity . This results in the formation of a wake flow at the cascade's trailing edge, which is illustrated in Figure 2. At station 3 of Figure 2, the non-homogeneous wake flow is accepted to turn into homogeneous due to turbulent mixing. This mixing generates additional total pressure losses. These losses can be calculated by continuity, momentum and energy equations [5].

Calculating trailing edge mixing loss is only necessary when profile loss coefficients are derived from boundary layer calculations, as experimental loss correlations already include these losses.

1.3.4 Exit Loss. The kinetic energy of mass flow which exits the turbine causes total energy loss, which means exit loss. In the multi-stage turbomachines, exit loss can be seen in only last stage. In the single stage turbomachine, the exit loss has a important effect on the decrease of the stage efficiency [5].

1.3.5 Trailing Edge Ejection Mixing Losses of Gas Turbine Blades. To increase gas turbine thermal efficiency, higher turbine inlet temperatures are required. The mixing losses are affected by cooling mass flow injected at the trailing edge, which is governed by factors such as angle and ejection velocity ratio. The efficiency of cooled turbine blades can be considerably decreased by choosing these parameters incorrectly [5].

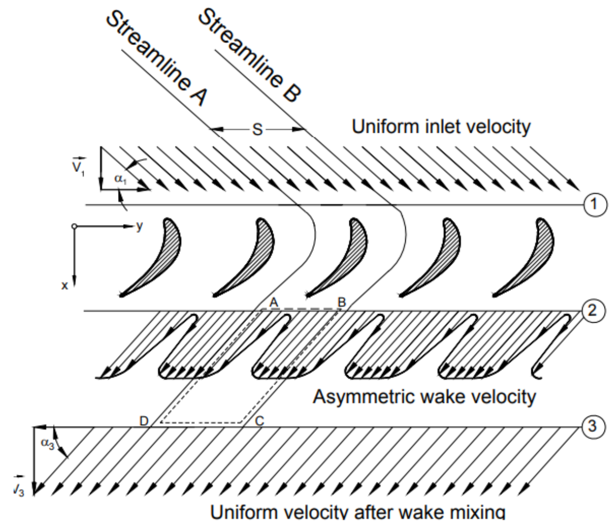

FIGURE 2: WAKE MIXING DOWNSTREAM OF A CASCADE WITH A FINITE TRAILING EDGE THICKNESS. [5]

1.4 Secondary Flows

When a rotating fluid particle undergoes turning, such as within a cascade, its rotational axis shifts in a direction perpendicular to the turning motion. This phenomenon, referred to as vorticity, describes the fluid's rotation and is represented as a vector aligned with the rotation axis. As the axis of rotation is deflected, a vorticity component aligns with the flow streamlines, which subsequently leads to the development of secondary flows.[7].

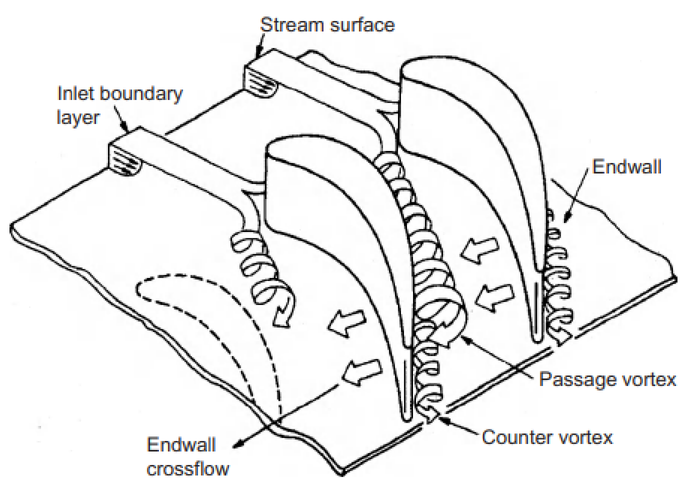

FIGURE 3: SECONDARY FLOW STRUCTURE WITHIN A BLADE PASSAGE [7]

The secondary flow pattern within a blade passage becomes more complex due to the flow behavior around the leading edge, as demonstrated in Figure 3 [7]. When the flow stands still, the vorticity within the annulus wall boundary layer is divided into two vortices, which are passage and counter vortex. Passage vortex enters the blade passage near the pressure surface, counter vortex enters beside the suction surface. Passage vortex is rapidly swept towards the suction surface by the cross-passage pressure gradient and counter vortex sticks to the suction surface hub.In addition to the vortices, the boundary layer fluid on the endwalls is driven from the pressure surface to the suction surface. This movement accumulates highly rotational fluid near the hub and casing endwalls on the suction surface, resulting in increased losses due to viscous shear and mixing. Downstream of the blades, this fluid contributes to the formation of a three-dimensional wake structure. [7].

The secondary flow situation happens in all axial turbomachines. In turbine components, huge amount of flow is rotating and high cross-passage pressure gradients cause to being stronger of secondary flows[7]. To minimize secondary flows near endwalls, researchers have studied on many design methods including skewed and swept blade profiling, editing to leading-edge near endwalls of blades, and non-axisymmetric endwall profiling. These methods, are used to make perfect the change of endwall boundary layers and pressure distribution of the endwalls as well as blade, thus achieve the reducing secondary flows with editing the geometry around endwalls[1].

1.4.1 Losses Due to Secondary Flows. "Endwall Loss The term "endwall loss" will be used in preference to "secondary loss" to describe all the loss arising on the annulus walls both within and outside of the blade passage. For turbines, endwall loss is a major source of lost efficiency, contributing typically 1/3 of the total loss."[8].

We mentioned that the primary cause of secondary flow is vorticities, with tip clearance vortices and hub and tip endwall vortices being the most significant contributors to substantial losses. Figure 4 schematically illustrates an overview of the hub and tip clearance vortices.

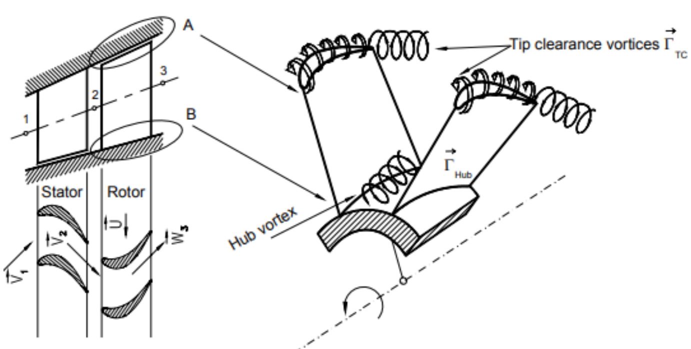

FIGURE 4: SCHEMATIC EXPLANATION OF SECONDARY FLOWS IN A TURBINE STAGE[5]

Tip Clearance Vortices: These vortices are generated as a result of pressure differences at the blade tip. The fluid particles near the blade tip tend to move from the pressure surface to the suction surface, forming a system of bound vortices. These vortices coalesce at the blade trailing edge and form a free vortex system.

"This movement triggers two mechanisms that contribute to efficiency and performance deterioration:
1) The tip clearance vortices induce drag forces and, thus, tip clearance secondary flow losses associated with an efficiency decrease of the turbo machinery stage.
2) The mass flow that escapes through the tip clearance does not contribute to the power generation thus causing a loss of turbine power."[5]

Endwall Secondary Flow Vortices: These vortices are formed as a result of the interaction between the low-energy endwall boundary layer and the pressure difference within the blade channel, very close to the endwall. Within the blade channel, there is a static pressure difference between the suction and pressure surface. In the mid-section of the channel where the high Reynolds number flow is assumed to be quasi potential flow, there is an equilibrium condition between the forces due to the above pressure differences and the convective flow forces.Near the side walls (hub or casing) where the boundary layer velocity distribution is affected by the viscosity, the low energetic boundary layer is not able to maintain this equilibrium condition[5].

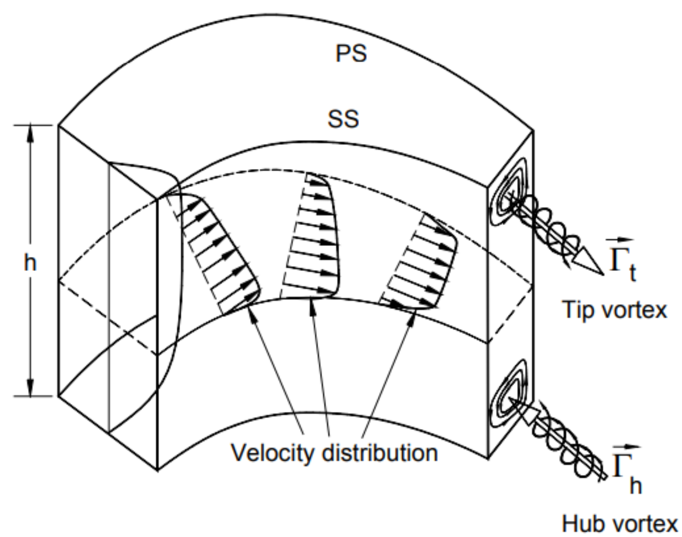

FIGURE 5: ENDWALL SECONDARY VORTICES AT THE HUB AND TIP [5]

Ultimately, the fluid particles in the boundary layers move from the pressure side (concave) to the suction side, forming secondary vortices in the blade hub and tip regions. This phenomenon is depicted in Figure 5. As shown, the circulation vectors of the two vortex systems point in opposite directions. These vortices generate a velocity field based on the Bio-Savart law(see at [[5], Sec.7.4.1]), inducing drag forces. To overcome these additional drag forces, convective forces must be applied, resulting in an increase in total pressure loss.

2. METHODOLOGY

2.1 T106A Turbine Blade Geometry

In this study, T106A cascade is used, which is taken from data of University of Cambiridge, Department of Engineering, Whittle Laboratory [9]. Table 1 includes design parameters of T106A cascade. Figure 6 illusturates the computational domain and boundary conditions in the x y plane.

TABLE 1:
SPECIFICATION OF T106A CASCADE

Parameter	Value
Chord (C)	198 mm
Axial chord (C_x)	170 mm
Pitch	158 mm
Span (b)	375 mm
Inlet angle (α_1)	45.5°
Design exit flow angle (α_2)	63.2°

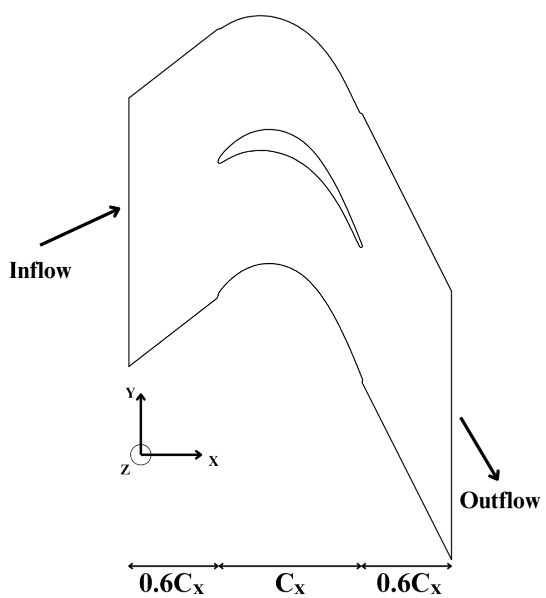

FIGURE 6: T106A TURBINE BLADE GEOMETRY

2.2 Mesh Specifications

2.2.1 2D Simulation.

Mesh Statistics

TABLE 2: 2D MESH STATISTICS

Average Element Size	Nodes	Elements
5e-3 (coarse)	14,981	14,545 (unstructured)
1e-3 (fine)	132,649	131,685(unstructured)

Figures 7 and 8 show close-up views of the three different meshes used in the simulations. Each figure highlights the overall mesh structure and the boundary layer region around the blade.

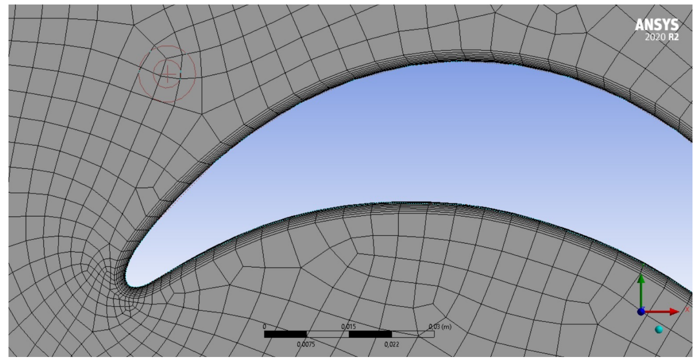

FIGURE 7: CLOSE-UP VIEW OF THE BOUNDAY LAYER MESH (COARSE MESH)

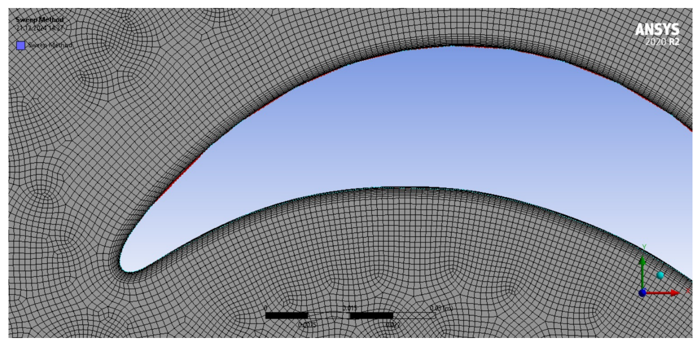

FIGURE 8: CLOSE-UP VIEW OF THE BOUNDAY LAYER MESH (FINE MESH)

A fine boundary layer mesh was created around the blade with the first cell height less than $Y^+ < 1$. The boundary layer mesh consisted of 10 layers with a growth rate of 1.2. The entire computational domain was meshed using quadrilateral (quad) elements.

Solution Setup

TABLE 3: FLOW SPECIFICATIONS

Parameter	Value
Inlet flow angle	45.5°
Total temperature at the inlet	312.9 K
Static pressure at the inlet	7340 Pa
Total pressure at the inlet	7770 Pa
Static pressure at the outlet	6950 Pa

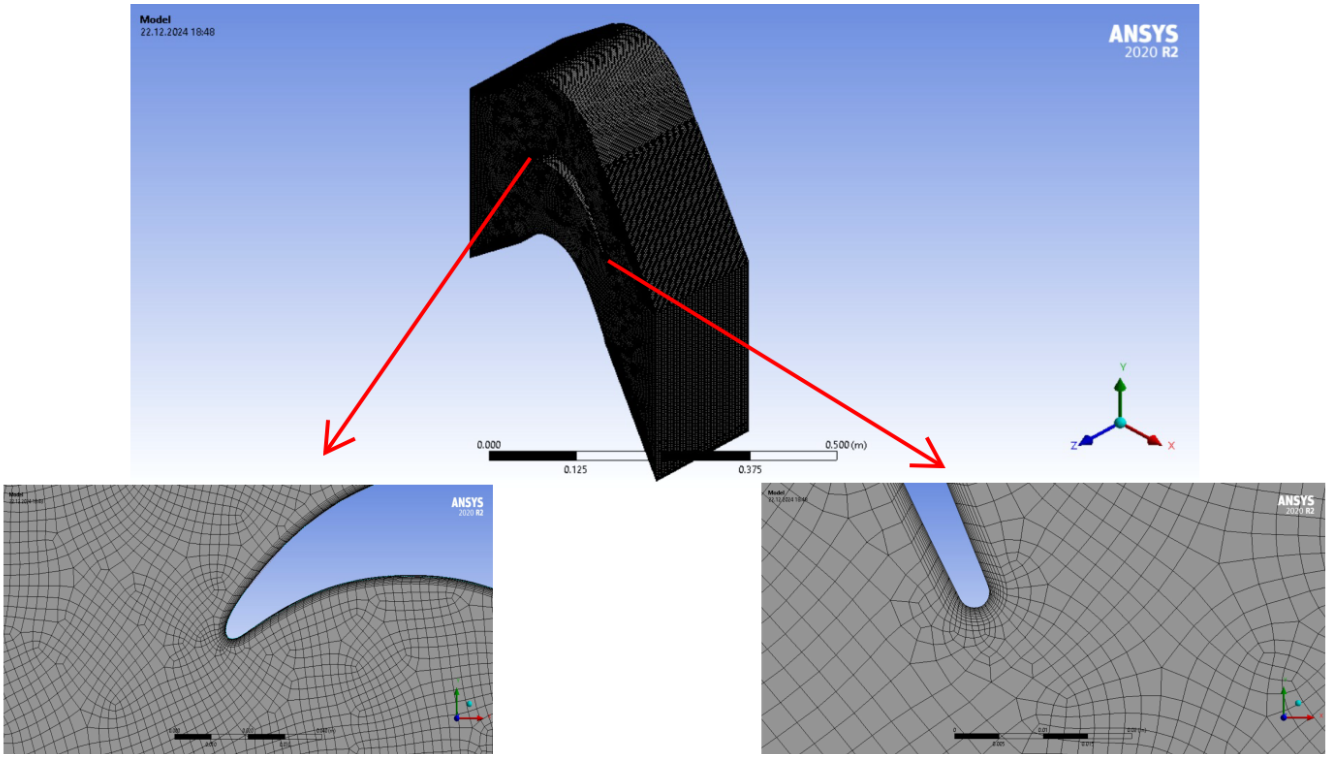

FIGURE 9: VIEW OF THE 3D MESH

Boundary Conditions: Velocity inlet boundary conditions were applied. When pressure inlet boundary conditions were used, the solution did not converge. Calculations were conducted at Reynolds numbers $Re = 60,000$ and $Re = 51,800$, based on the inlet velocity and axial chord length. Periodic boundary conditions were applied on the blade side surfaces to account for the effects of neighboring blades on the flow field. No slip wall boundary conditions were applied to blade surface. Pressure outlet boundary condition were applied.

Turbulence Models Used

Simulations were performed using different turbulence models:

- **Spalart-Allmaras (SA)**
- **k-ϵ**
- **k-ω SST** (did not converge for this case)

2.2.2 3D Simulation.

Mesh Statistics

TABLE 4: 3D MESH STATISTICS

Average Element Size	Nodes	Elements
5e-3 (coarse)	1,200,952	1,150,875 (unstructured)
2.5e-3 (fine)	2,422,804	2,347,050 (unstructured)

Boundary Conditions:

- Periodic boundary conditions were applied on the blade side surfaces to include the effects of neighboring blades on the flow field.
- Half-span was used for 3D simulations, taking advantage of the symmetry plane boundary condition to reduce the computation time.
- Both pressure inlet and velocity inlet boundary conditions were applied.

Reynolds Number: $Re = 60,000$ based on axial chord length and inlet velocity.

A close-up view of the 3D mesh can be seen in Figure 7.

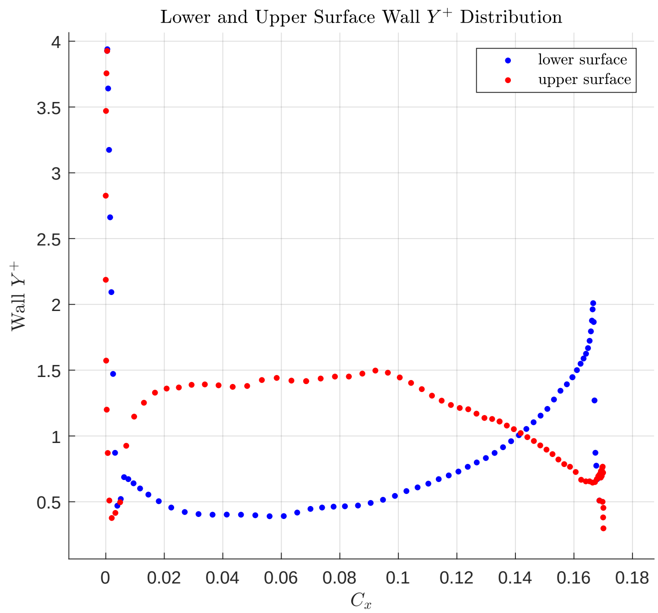

FIGURE 10: WALL Y^+ DISTRIBUTION OVER AXIAL CHORD

In Figure 10 wall Y^+ values along axial chord are shown.

Solution Setup

TABLE 5: FLOW SPECIFICATIONS

Parameter	Value
Inlet flow angle	45.5°
Total temperature at the inlet	312.9 K
Static pressure at the inlet	7340 Pa
Total pressure at the inlet	7770 Pa
Static pressure at the outlet	6950 Pa

2.3 Spalart Allmaras Turbulence Model

The Spalart-Allmaras model is a single-equation turbulence model designed to simulate turbulent flows. Instead of solving for turbulent kinetic energy directly, it works on a modified turbulent viscosity. The model is particularly useful for flows dominated by boundary layers and provides acceptable results with low computational cost, making it highly suitable for aerodynamic and external flow analyses [10].

Mathematical Model

Turbulent eddy viscosity ν_t defined as follows:

$$\nu_t = \tilde{\nu} f_{v1}$$

Function f_{v1} given as:

$$f_{v1} = \frac{\chi^3}{\chi^3 + C_{v1}^3}$$

and intermediate variable χ given as:

$$\chi = \frac{\tilde{\nu}}{\nu}$$

The fundamental transport equation form of the Spalart-Allmaras model is expressed as follows:

$$\frac{\partial \tilde{\nu}}{\partial t} + u_j \frac{\partial \tilde{\nu}}{\partial x_j} = C_{b1}[1 - f_{t2}]\tilde{S}\tilde{\nu} + \frac{1}{\sigma}\left\{\nabla \cdot [(\nu + \tilde{\nu})\nabla\tilde{\nu}] + C_{b2}|\nabla\tilde{\nu}|^2\right\}$$
$$-\left[C_{w1} f_w - \frac{C_{b1}}{\kappa^2} f_{t2}\right]\left(\frac{\tilde{\nu}}{d}\right)^2 + f_{t1}\Delta U^2$$

Where modified deformation tensor $\tilde{S}$ and function f_{v2} is:

$$\tilde{S} \equiv S + \frac{\tilde{\nu}}{\kappa^2 d^2} f_{v2}$$

$$f_{v2} = 1 - \frac{\chi}{1 + \chi f_{v1}}$$

Where:

$$S \equiv \sqrt{2\Omega_{ij}\Omega_{ij}}$$

$$\Omega_{ij} \equiv \frac{1}{2}\left(\frac{\partial u_i}{\partial x_j} - \frac{\partial u_j}{\partial x_i}\right)$$

$$f_w = g\left[\frac{1 + C_{w3}^6}{g^6 + C_{w3}^6}\right]^{1/6}$$

$$g = r + C_{w2}(r^6 - r)$$

$$r \equiv \frac{\tilde{\nu}}{\tilde{S}\kappa^2 d^2}$$

$$f_{t1} = C_{t1} g_t \exp\left(-C_{t2}\frac{\omega_t^2}{\Delta U^2}\left[d^2 + g_t^2 d_t^2\right]\right)$$

$$f_{t2} = C_{t3}\exp(-C_{t4}\chi^2)$$

Constants used in model given in Table 6.

Advantages and Limitations

Advantages include: single-equation structure reduces computational cost,it delivers high accuracy for flows dominated by boundary layers and compatible with wall functions in high Reynolds number flows.

Limitations include: Limited accuracy in modeling separation and reattachment regions, less effective for internal flows and turbulence-shock interactions and requires modifications to model transitional flows.

TABLE 6:
MODEL CONSTANTS FOR SPALART-ALLMARAS MODEL

Parameter	Value
σ	2/3
C_{b1}	0.1355
C_{b2}	0.622
κ	0.41
C_{w1}	$C_{b1}/\kappa^2 + 1 + C_{b2}/\sigma$
C_{w2}	0.3
C_{w3}	2
C_{v1}	7.1
C_{t1}	1
C_{t2}	2
C_{t3}^*	1.2
C_{t4}^*	0.5

* C_{t3} and C_{t4} values are given for model version II [10].

2.4 K-Epsilon Turbulence Model

The k-epsilon model is one of the most widely used turbulence models. As a two-equation model, it incorporates two additional transport equations to describe the turbulent characteristics of the flow. This enables it to account for past effects such as the convection and diffusion of turbulent energy.

The first variable it transports is the turbulent kinetic energy, k. The second is the turbulent dissipation, ϵ, which determines the turbulence scale, while k represents the energy within the turbulence.There are two primary versions of the $k-\epsilon$ model [11, 12]. The formulation by Launder and Sharma is commonly referred to as the "Standard" $k-\epsilon$ Model. The model was originally developed to enhance the mixing-length approach and to provide an alternative to algebraically defining turbulence length scales in moderately to highly complex flows. Mathematical model for standard k-epsilon given in following.

Mathematical Model

Turbulent viscosity is given as:

$$\mu_t = \rho C_\mu \frac{k^2}{\epsilon}$$

Transport equation for turbulent kinetic energy k:

$$\frac{\partial}{\partial t}(\rho k) + \frac{\partial}{\partial x_i}(\rho k u_i)$$
$$= \frac{\partial}{\partial x_j}\left[\left(\mu + \frac{\mu_t}{\sigma_k}\right)\frac{\partial k}{\partial x_j}\right] + P_k + P_b - \rho\epsilon - Y_M + S_k$$

Transport equation for turbulent dissipation ϵ:

$$\frac{\partial}{\partial t}(\rho \epsilon) + \frac{\partial}{\partial x_i}(\rho \epsilon u_i)$$
$$= \frac{\partial}{\partial x_j}\left[\left(\mu + \frac{\mu_t}{\sigma_\epsilon}\right)\frac{\partial \epsilon}{\partial x_j}\right] + C_{1\epsilon}\frac{\epsilon}{k}(P_k + C_{3\epsilon}P_b) - C_{2\epsilon}\rho\frac{\epsilon^2}{k} + S_\epsilon$$

Where, Production term P_k, representing the generation of turbulent kinetic energy due to velocity gradients:

$$P_k = -\rho\overline{u_i'u_j'}\frac{\partial u_j}{\partial x_i}$$

$$P_k = \mu_t S^2$$

Where S is modulus of the mean rate-of-strain tensor, given as:

$$S \equiv \sqrt{2S_{ij}S_{ij}}$$

Turbulence production due to buoyancy effects represented by P_b as:

$$P_b = \beta g_i \frac{\mu_t}{\mathrm{Pr}_t}\frac{\partial T}{\partial x_i}$$

Where Pr_t is turbulent Prandtl number for energy, g_i is gravitational vector component in the ith direction and β is coefficient of thermal expansion defined as:

$$\beta = -\frac{1}{\rho}\left(\frac{\partial \rho}{\partial T}\right)_p$$

The default value for Pr_t in standart model is 0.85 and constants used in standart model given in Table 7.

TABLE 7:
MODEL CONSTANTS FOR k-ϵ MODEL

Parameter	Value
$C_{1\epsilon}$	1.44
$C_{2\epsilon}$	1.92
C_μ	0.09
σ_k	1.0
σ_ϵ	1.3

* $C_{3\epsilon}$ value is depends on the flow characteristics. For RDT-based compression term see reference [13] .

Advantages and Limitations

Advantages include: Applicable to a wide range of flow conditions, including free shear flows and wall-bounded flows, balances computational cost and accuracy, making it suitable for industrial applications, model relies on a limited set of empirical constants, simplifying implementation and interpretation.

Limitations include: Requires fine meshes near walls or wall functions for accurate boundary layer modeling, struggles to capture complex flow phenomena like flow separation and reattachment accurately, not suitable for modeling laminar-to-turbulent transition without modifications and performing insufficiently in cases of large adverse pressure gradients [14].

2.5 K-Omega Turbulence Model

The k-Omega ($k-\omega$) turbulence model is one of the most widely used methods in fluid mechanics to model and understand the complex dynamics of turbulence. This model operates by solving two transport equations, one for the turbulent kinetic energy (k) and the other for the specific dissipation rate (ω). The turbulent kinetic energy quantifies the energy contained in the velocity fluctuations of the flow, while the specific dissipation rate represents how quickly this energy dissipates into heat due to viscous effects at smaller scales. The $k-\omega$ model is particularly effective in predicting boundary layer behaviors and is well-suited for low Reynolds number flows, where viscous effects play a significant role. These advantages make it a powerful tool in engineering and scientific applications. However, its sensitivity to free-stream conditions in regions away from walls poses a limitation, especially in flows with significant freestream turbulence. To address these shortcomings and expand its applicability, the SST (Shear Stress Transport) $k-\omega$ model was developed [15]. The SST model combines the strengths of the standard $k-\omega$ and $k-\epsilon$ models through a hybrid formulation. Near the wall regions, it leverages the accuracy of the $k-\omega$ model, while in the free-stream regions, it transitions to the $k-\epsilon$ model to mitigate sensitivity to inflow conditions. This blending is achieved using a carefully designed interpolation function, making the SST model robust across a wide range of flow scenarios. Mathematical model for SST $k-\omega$ given in following.

Mathematical Model

Kinematic eddy viscosity given as:

$$\nu_T = \frac{a_1 k}{\max(a_1\omega, SF_2)}$$

Where the F_2 is second blending function and given as:

$$F_2 = \tanh\left[\left(\max\left(\frac{2\sqrt{k}}{\beta^*\omega y'}, \frac{500\nu}{y^2\omega}\right)\right)^2\right]$$

Transport Equation for Turbulent Kinetic Energy k:

$$\frac{\partial k}{\partial t} + U_j\frac{\partial k}{\partial x_j} = P_k - \beta^* k\omega + \frac{\partial}{\partial x_j}\left[(\nu + \sigma_k\nu_T)\frac{\partial k}{\partial x_j}\right]$$

Where P_k is rate of energy transfer from the mean flow to turbulence, with a limit to avoid excessive values and given as:

$$P_k = \min\left(\tau_{ij}\frac{\partial U_i}{\partial x_j}, 10\beta^* k\omega\right)$$

Transport Equation for Specific Dissipation Rate ω:

$$\frac{\partial \omega}{\partial t} + U_j\frac{\partial \omega}{\partial x_j}$$

$$= \alpha S^2 - \beta\omega^2 + \frac{\partial}{\partial x_j}\left[(\nu + \sigma_\omega\nu_T)\frac{\partial \omega}{\partial x_j}\right] + 2(1-F_1)\omega_2\frac{1}{\omega}\frac{\partial k}{\partial x_i}\frac{\partial \omega}{\partial x_i}$$

Where F_1 is blending function given as:

$$F_1 = \tanh\left\{\left\{\min\left[\max\left(\frac{\sqrt{k}}{\beta^*\omega y'}, \frac{500\nu}{y^2\omega}\right), \frac{4\sigma_{\omega2}k}{CD_{k\omega}y^2}\right]\right\}^4\right\}$$

And $CD_{k\omega}$ is A correction term that accounts for the interaction between k and ω gradients given as:

$$CD_{k\omega} = \max\left(2\rho\sigma_{\omega2}\frac{1}{\omega}\frac{\partial k}{\partial x_i}\frac{\partial \omega}{\partial x_i}, 10^{-10}\right)$$

Constants used in SST model given in Table 8.

TABLE 8:
MODEL CONSTANTS FOR k-ω SST MODEL

Parameter	Value
α_1	5/9
α_2	0.44
β_1	3/40
β_2	0.0828
β^*	9/100
σ_{k1}	0.85
σ_{k2}	1.0
$\sigma_{\omega1}$	0.5
$\sigma_{\omega2}$	0.856

Advantages and Limitations

Advantages include: By combining the strengths of k-omega and k-epsilon models, the SST model provides a comprehensive solution that adapts to the specific turbulence characteristics of different flow regions.Unlike some other turbulence models, the SST model does not rely on wall functions, enabling it to resolve near-wall flows more naturally and flexibly. The model offers improved accuracy in predicting separated flows and flows with adverse pressure gradients, which are challenging for many other turbulence models. Its ability to handle a wide range of flow conditions without compromising stability or accuracy makes the SST model a preferred choice in industrial and academic simulations.

Limitations include: Accurately resolving the near-wall region requires fine grid spacing, leading to increased computational cost, especially in large-scale or three-dimensional simulations. The model's performance can be influenced by the specification of free-stream turbulence properties, such as turbulence intensity and length scale. For flows involving intricate geometries or high curvature, additional attention to mesh generation and model tuning may be required.

2.6 Comparison of Results

In this section, the simulations are compared with experimental data. Firstly, the results obtained from two-dimensional analyses are presented with graphs, and their agreement with experimental data is evaluated. Subsequently, the data from three-dimensional analyses are examined in a similar manner, with detailed comparisons provided. Relevant comments are included under each graph to draw conclusions about the accuracy of the simulation results and their consistency with experimental data. This approach offers a comprehensive assessment of the performance and accuracy of analyses conducted in different dimensions.

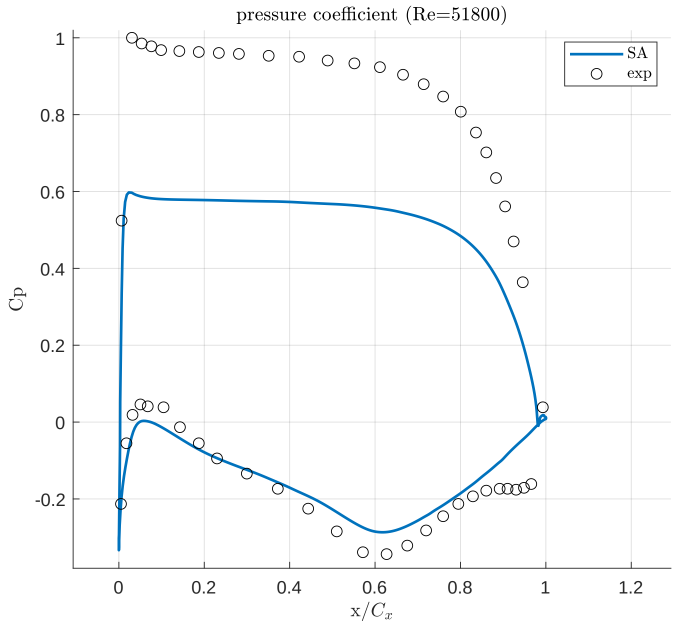

FIGURE 11: 2D C_p VS X/C_x , Re= 51800, SA MODEL

2.6.1 Analysis of 2D Results . In these simulations, the pressure coefficient distributions were obtained at two different Reynolds numbers: Re=60000 and Re=51800. Both cases were solved using the Spalart-Allmaras (SA) turbulence model, and the only parameter changed between the simulations was the velocity inlet value, as the Reynolds number was calculated based on the inlet velocity. No other boundary condition or parameter was modified.

In Figure 12 it could be seen that with Re=60000, the numerical results demonstrate a reasonable agreement with the experimental data, accurately capturing the trends in the pressure distribution. However in Figure 11 with Re=51800, the results deviate significantly, especially in regions affected by adverse pressure gradients, which are critical for flow separation.

The discrepancies observed at Re=51800 can be attributed to the absence of a transition model in the simulations. This deviation underscores the significance of accurately representing the transition from laminar to turbulent flow. Transition modeling is essential in such cases as it directly impacts the prediction of flow separation and reattachment, particularly at lower Reynolds numbers where transition effects are more pronounced.

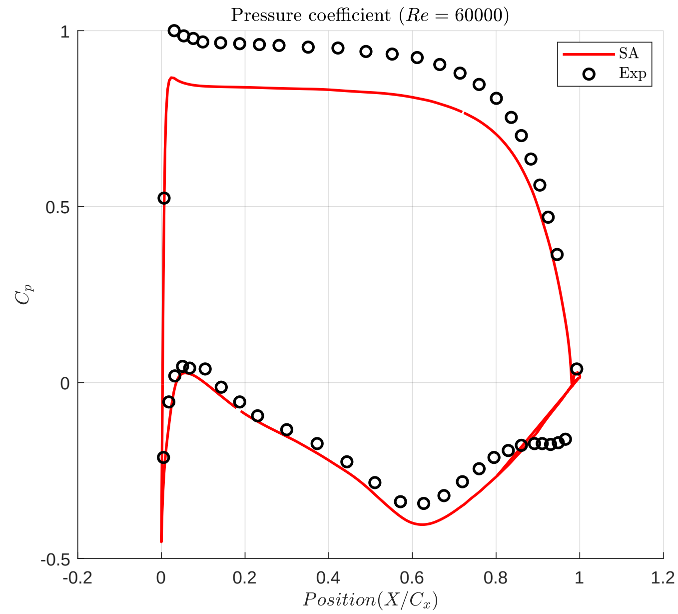

FIGURE 12: 2D C_p VS X/C_x , Re=60000, SA MODEL

The SA model, being a fully turbulent model, does not account for laminar-turbulent transition, which likely led to the underprediction of flow separation behavior in the Re=51800 case. To improve accuracy, incorporating a transition model capable of capturing these effects is essential, as it would better replicate the boundary layer development and flow separation phenomena in such cases.

In future work, we aim to use a transition model to better capture laminar-turbulent transition effects, enhancing flow physics representation and simulation accuracy.

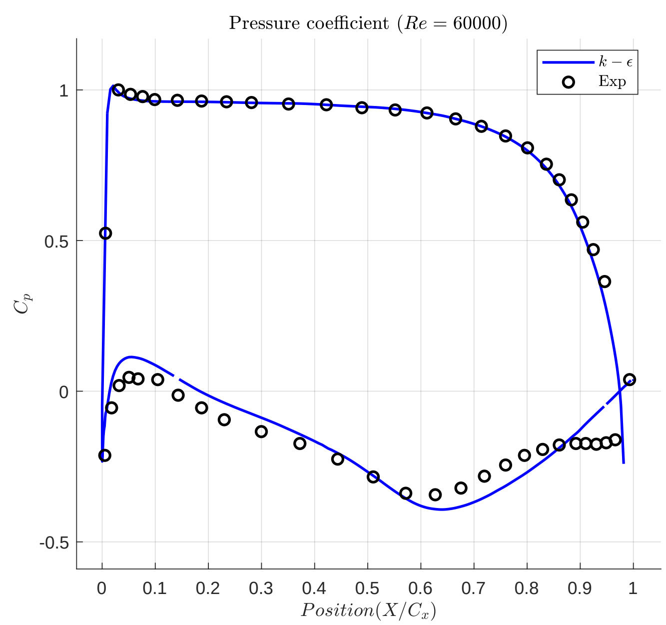

FIGURE 13: 2D C_p VS X/C_x , Re=60000, $k-\epsilon$ MODEL

In Figure 13 it could be seen that $k-\epsilon$ model tends to perform well in attached flow regions and mild adverse pressure gradients. At Re = 60,000, the boundary layer might remain attached or exhibit minimal separation, enabling the model to capture the Cp distribution trends accurately.

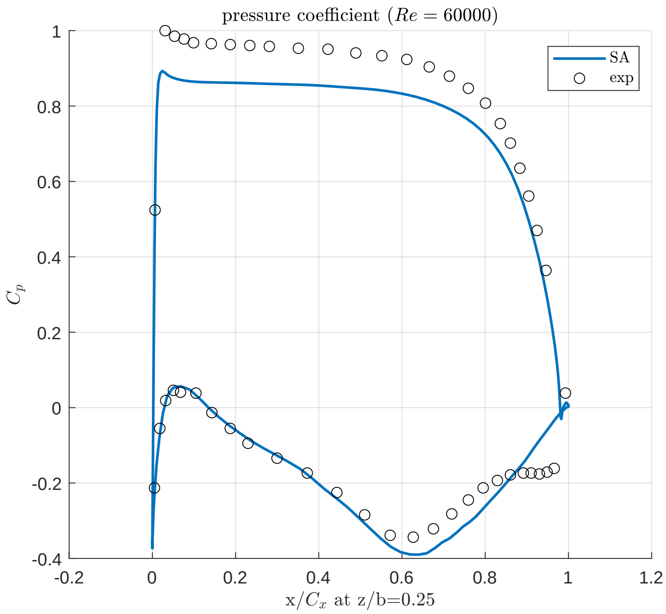

FIGURE 14: 3D C_p VS X/C_x, z/b=0.25, Re=60000, SA MODEL

2.6.2 Analysis of 3D Results. In the simulations, a turbulence intensity of 2% was specified when employing the velocity inlet boundary condition. However, this choice may not have adequately captured the development of turbulent flow, as well as the flow's separation and reattachment behavior, particularly in the case where the Reynolds number is 60,000.

The velocity inlet boundary condition operates under the assumption of a fully turbulent flow at the inlet. However, an improper selection of a critical parameter such as turbulence intensity can lead to significant deviations from experimental data, even at relatively high Reynolds numbers, such as 60,000. As a result, adopting an alternative approach, such as the pressure inlet boundary condition, may allow for a more accurate representation of the natural evolution of turbulence, thereby reducing these discrepancies.

3. RESULTS AND DISCUSSION

3.1 Discussion of 3D C_p Results

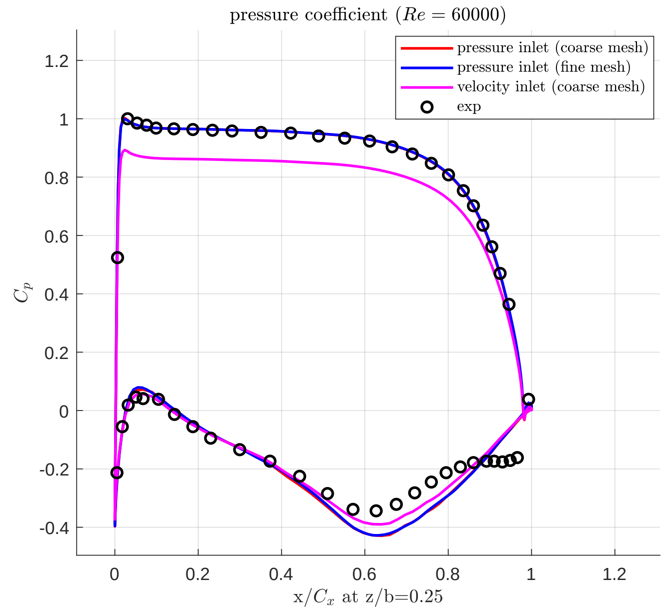

FIGURE 15: 3D C_p VS X/C_x COMPARISONS

3D simulations using the pressure inlet boundary condition and velocity inlet boundary condition were performed and the results were compared. the results can be seen in Figure 15. Pressure inlet allowed the turbulence parameters to more accurately represent the natural evolution of the flow. Since the inlet pressure, turbulence kinetic energy and turbulence dissipation rate were calculated more accurately in this boundary condition, the results were much closer to the experimental data. Flow separation and reconnection phenomena, especially in regions with adverse pressure gradients, could be modeled more realistically with pressure inlet.

This comparison showed that the pressure inlet boundary condition can produce more consistent and reliable results, especially at high Reynolds numbers and turbulent flows. In conclusion, the pressure inlet boundary condition allowed us to achieve better agreement with experimental data while ensuring accurate modeling of turbulence.

A meshing dependency study was also performed and the same results were obtained regardless of the mesh size.

3.2 Pressure and Velocity distributions

In order to visualize the pressure and velocity distributions, a cross section was taken in three-dimensional space. The pressure distribution can be seen in Figure 16 and the velocity distribution in Figure 17.

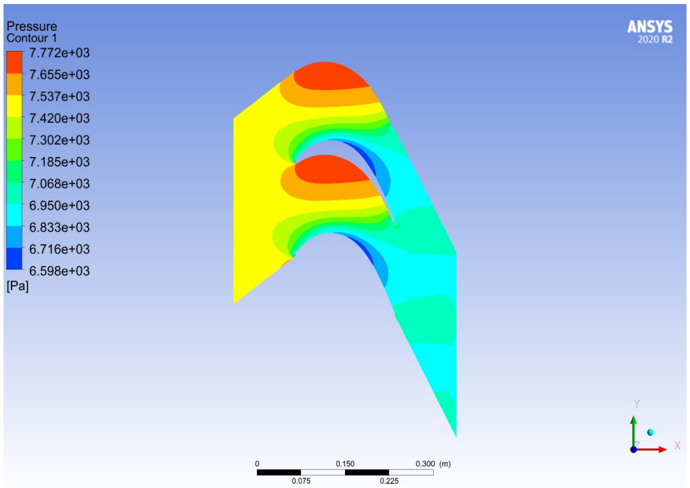

FIGURE 16: PRESSURE DISTRIBUTION

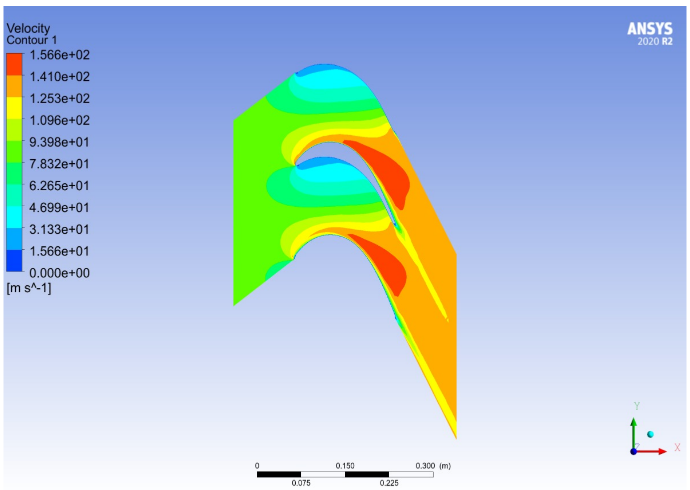

FIGURE 17: VELOCITY DISTRIBUTION

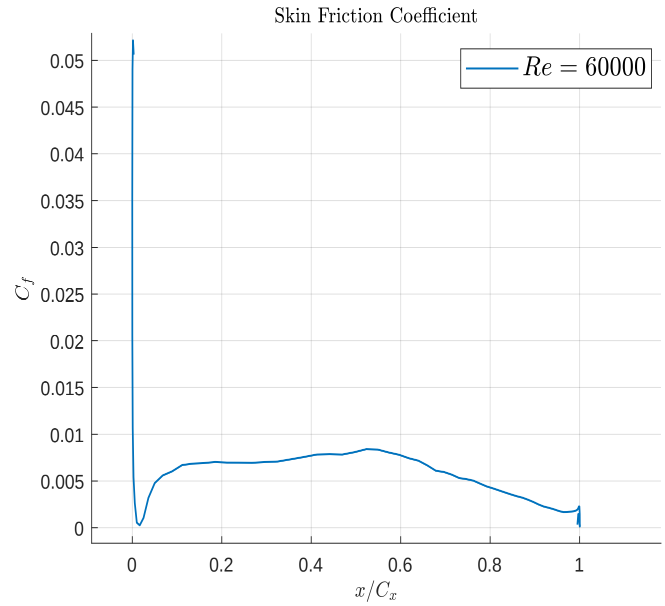

FIGURE 18: SKIN FRICTION COEFFICIENT VS X/C_x FOR UPPER SURFACE

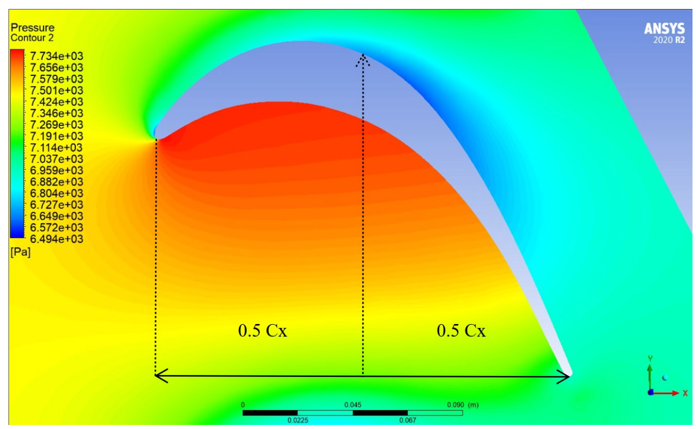

FIGURE 19: PRESSURE DISTRIBUTION FOCUSED ON FLOW SEPARATION

3.3 Discussion of 3D C_f Results

To investigate the flow on the suction side of the blade, the skin friction coefficient, defined as

$$C_f = \frac{\tau_w}{\frac{1}{2}\rho_{\text{in}} u_{\text{in}}^2}$$

is presented in Figure 18. Here, τ_w denotes the wall shear stress. The friction coefficient begins to decline at $x/C_x = 0.55$, indicating the onset of boundary layer separation. This finding is further supported by the region of constant pressure associated with flow recirculation downstream of the separation, as seen on the rear portion of the blade in Figure 14. Additionally, the suction-side separation bubble is evident from the pressure distribution shown in Figure 19 [16].

Flow separation is when the flow, usually moving rapidly along the surface, becomes dislodged due to the slope or shape of the surface. This prevents the flow from continuing smoothly parallel to the surface and leads to a region often referred to as the "turbulent zone". After this region, the flow starts to move in the opposite direction.

In the region of reverse flow at the surface, the pressure usually increases. The rupture of the flow reduces the speed of the air flow, which causes the pressure to increase see at Figure 16.

Downstream of the separation region, the free shear within the separation bubble becomes unstable via the Kelvin-Helmholtz mechanism, leading to a full transition to turbulence and subsequent boundary layer reattachment. This reattachment can be observed from the temporally averaged skin friction coefficient, which becomes positive near the trailing edge (TE). This phenomenon begins to occur around $x/C_x = 0.95$ and can be Figure 18.

3.4 Discussion of 3D KE loss coefficient Results

Figure 20 shows the linear cascade at a distance $0.4C_x$ with all y-axis values. Moving to Figure 21, a zoom-in of the previous figure is presented, focusing on the upper and lower parts of the cascade and highlighting the effect of the single blade on the flow characteristics.

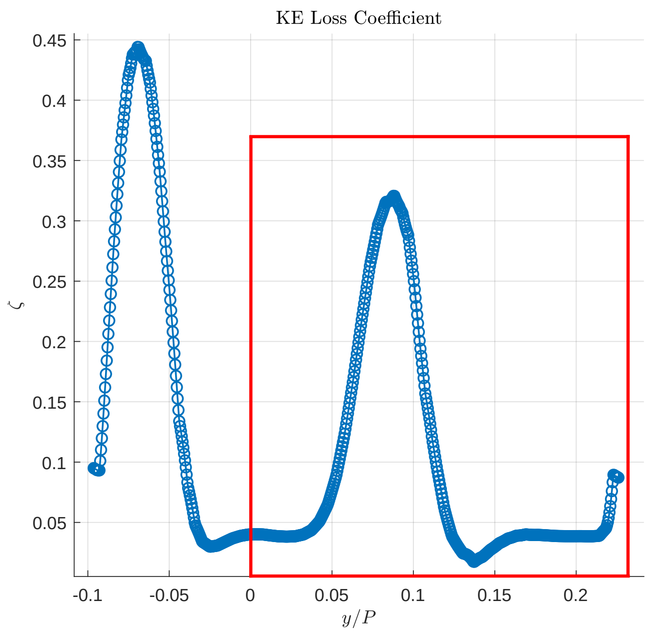

FIGURE 20: KINETIC ENERGY LOSS COEFFICIENT VS Y/P

The kinetic energy loss coefficient (ζ) [16] is defined as follows according to the given formulation:

$$\zeta = \frac{p_{t,\text{in}} - \bar{p}_{t,\text{out}}}{p_{t,\text{in}} - p_{\text{ref}}}$$

This expression calculates the losses by normalizing the difference between the total pressure at the inlet ($p_{t,\text{in}}$) and the average total pressure at the outlet ($\bar{p}_{t,\text{out}}$) to the reference pressure (p_{ref}), see at Figure 20. The losses are determined by measuring $\bar{p}_{t,\text{out}}$ for the linear cascade at a distance $0.4C_x$ from the trailing edge (TE) line. This approach is a standard method for understanding the energy losses in the separation, mixing, and wake region of the flow over the wing.

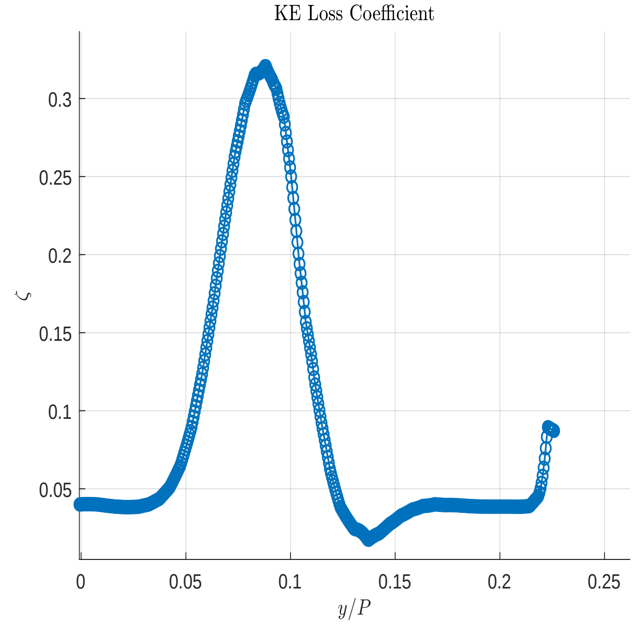

FIGURE 21: KINETIC ENERGY LOSS COEFFICIENT VS Y/P

Based on the use of the formula, the trend in the graph can be explained as follows:

1. **Peak of Loss Coefficient:**
   - ζ reaches a maximum value in the wake region ($y/P \approx 0.1$). This indicates that the mixing and turbulence in the wake region causes a significant drop in the total pressure.
2. **Decline and Stabilization:**
   - Once outside the wake region ($y/P > 0.15$), the losses decrease rapidly. It is seen that the flow stabilizes and the losses remain at a low level.
3. **Exit Zone:**
   - The small increase of the loss coefficient outside the wake region ($y/P > 0.2$) may reflect the small turbulence effects during flow reorganization in the non-wake regions, as indicated by the LES and DNS modeling.

4. CONCLUSION

This study comprehensively investigates the aerodynamic performance of the T106A low-pressure turbine cascade using steady-state CFD simulations. By analyzing pressure coefficient distributions, kinetic energy losses, and flow separation phenomena, the research provides valuable insights into turbine blade design and performance prediction. The simulations were conducted using Spalart-Allmaras, k-epsilon, and k-omega turbulence models, with each model's strengths and weaknesses being observed.

The Spalart-Allmaras model proved effective for high Reynolds number flows, but due to its inability to accurately model the laminar-to-turbulent transition, it yielded errors in low Reynolds number conditions. This limitation led to inaccuracies in regions where the flow underwent a laminar-to-turbulent transition. The k-epsilon model produced satisfactory results in attached flow regions, but struggled with flow separation, particularly in areas with sharp adverse pressure gradients. The k-omega model successfully predicted flow separation and turbulence but showed some challenges in high Reynolds number flows.

The pressure coefficient distributions followed expected trends in attached flow regions, while a sharp drop in pressure was observed in flow separation areas, indicating significant energy losses. Kinetic energy losses were more pronounced downstream of the blades, where the flow detached and formed turbulent wakes.

The use of transition models played a critical role in improving the prediction accuracy, especially in low Reynolds number flows where laminar-to-turbulent transition is common. Additionally, the pressure inlet boundary condition was found to better capture the natural development of turbulence, providing more accurate results, especially in high Reynolds number cases, and matching experimental data more closely.

The mesh dependency analysis confirmed the robustness of the simulation methodology, ensuring consistent results across different computational setups. This analysis was important for verifying the reliability of the simulation approach.

In conclusion, this study emphasizes the importance of selecting appropriate turbulence models and incorporating transition modeling to accurately predict aerodynamic performance in turbine cascades. Future research should focus on more advanced transition models and unsteady flow simulations to better capture the complexities of flow dynamics, which could further improve the aerodynamic efficiency of low-pressure turbines.

ACKNOWLEDGMENTS

We would like to express our sincere gratitude to Asst. Prof. Oğuzhan Murat for his invaluable guidance, encouragement, and support throughout this study. His expertise and dedication have been instrumental in shaping the direction and quality of this work. We also thank Seyfullah Çay for his helpful feedback during this research.

REFERENCES

[1] Zhengping Zou, Huoxing Liu Weihao Zhang, Songtao Wang. *Axial Turbine Aerodynamics for Aero-Engines: Flow Analysis and Aerodynamics Design*, 1st ed. Springer (2018): pp. 15–16,143–144.

[2] Rolls-Royce. *The Jet Engine*, 5th ed. Technical Publications Department, Rolls-Royce plc, Derby, England (1996): p. 47.

[3] Hodson, Howard P. and Howell, Robert J. "The Role of Transition in High-Lift Low-Pressure Turbines for Aeroengines." *Progress in Aerospace Sciences* Vol. 41 (2005): p. 419454. DOI 10.1016/j.paerosci.2005.08.001.

[4] Yıldırım, Emre. "Hydrodynamic Analysis of Gas Turbine Blades." Master's Thesis, Gazi University, Graduate School of Natural and Applied Sciences, Ankara, Turkey. 2022. M.Sc. Thesis.

[5] Schobeiri, Meinhard T. *Turbomachinery Flow Physics and Dynamic Performance*, 2nd ed. Springer (2012): .

[6] Traupel, Walter. *Thermische Turbomaschinen: Erster Band Thermodynamisch-Strömungstechnische Berechnung*. Springer (1977).

[7] Dixon, S.L. and Hall, Cesare. *Fluid Mechanics and Thermodynamics of Turbomachinery*, 7th ed. Butterworth-Heinemann (2014): pp. 245–248.

[8] Denton, J. D. "The 1993 IGTI Scholar Lecture: Loss Mechanisms in Turbomachines." *ASME Journal of Turbomachinery* Vol. 115 No. 4 (1993): pp. 621–656. DOI 10.1115/1.2929299.

[9] of Cambridge, University. "T106 Test Case - Axial Turbine Cascade." http://www-g.eng.cam.ac.uk/whittle/T106/Start.html. Accessed: December 21, 2024.

[10] Spalart, Philippe and Allmaras, Steven. "A One-Equation Turbulence Model for Aerodynamic Flows." *AIAA Journal* Vol. 439 (1992). DOI 10.2514/6.1992-439.

[11] Jones, W.P and Launder, Brian. "The Prediction of Laminarization with a Two-Equation Model of Turbulence." *International Journal of Heat and Mass Transfer* Vol. 15 (1972): pp. 301–314. DOI 10.1016/0017-9310(72)90076-2.

[12] Launder, B.E. and Sharma, B.I. "Application of the Energy-Dissipation Model of Turbulence to the Calculation of Flow Near a Spinning Disc." *Letters in Heat and Mass Transfer* Vol. 1 No. 2 (1974): pp. 131–137. DOI 10.1016/0094-4548(74)90150-7.

[13] Tahry, Sherif H. El. "K-Epsilon Equation for Compressible Reciprocating Engine Flows." *Journal of Energy* Vol. 7 (1983): pp. 345–353.

[14] Wilcox, David C. *Turbulence Modeling for CFD*, 2nd ed. Dcw Industries, Incorporated (1998): pp. 173–175.

[15] Menter, Florian R. "Zonal Two Equation k-w Turbulence Models for Aerodynamic Flows." *Proceedings of the ASME IDETC/CIE*. 1993.

[16] Fiore, Maxime, Gojon, Romain, Mischlich, Gonzalo Sáez and Gressier, Jérémie. "LES of the T106 low-pressure turbine: Spectral proper orthogonal decomposition of the flow based on a fluctuating energy norm." *Computers and Fluids* Vol. 252 (2023): p. 105761. DOI 10.1016/j.compfluid.2022.105761. URL https://hal.science/hal-04067050.

[17] Saha, Geetam and Ranjan, Rajesh. "Transition Modelling for Flow Separation in Low-Pressure Turbine Cascades." *Proceedings of the 48th National Conference on Fluid Mechanics and Fluid Power (FMFP)*. FMFP2021-10-068. 2021. BITS Pilani, Pilani Campus, RJ, India.

[18] Karahan, Cay S., D. T. and Gungor, A. G. "Investigation of end-wall effects on low-pressure turbines by using large eddy simulation." *VII European Congress on Computational Methods in Applied Sciences and Engineering (ECCOMAS 2016)*. 2016. Crete, Greece.

[19] Cay, Karahan D. T., S. and Gungor, A. G. "Large eddy simulation of end wall flows in low pressure turbines." *9th International Conference on Computational Fluid Dynamics (ICCFD9)*. ICCFD9-2016-211. 2016. Istanbul, Turkey.

[20] Cay, S. and Gungor, A. G. "Numerical investigation of inlet boundary condition effects on secondary flows in low pressure turbines." *9th Ankara International Aerospace Conference (AIAC-2017-068)*. 2017. Ankara, Turkey.